ADVANCED MATERIALS
www.advmat.de

Discovery of Real-Space Topological Ferroelectricity in Metallic Transition Metal Phosphides

Xian-Kui Wei, Gustav Bihlmayer, Xiaodong Zhou, Wanxiang Feng, Yury V. Kolen'ko, Dehua Xiong, Lifeng Liu, Stefan Blügel, and Rafal E. Dunin-Borkowski*

Ferroelectric metals—with coexisting ferroelectricity and structural asymmetry—challenge traditional perceptions because free electrons screen electrostatic forces between ions, the driving force of breaking the spatial inversion symmetry. Despite ferroelectric metals having been unveiled one after another, topologically switchable polar objects with metallicity have never been identified so far. Here, the discovery of real-space topological ferroelectricity in metallic and non-centrosymmetric Ni_2P is reported. Protected by the rotation–inversion symmetry operation, it is found that the balanced polarity of alternately stacked polyhedra couples intimately with elemental valence states, which are verified using quantitative electron energy-loss spectroscopy. First-principles calculations reveal that an applied in-plane compressive strain creates a tunable bilinear double-well potential and reverses the polyhedral polarity on a unit-cell scale. The dual roles of nickel cations, including polar displacement inside polyhedral cages and a 3D bonding network, facilitate the coexistence of topological polarity with metallicity. In addition, the switchable in-plane polyhedral polarity gives rise to a spin–orbit-coupling-induced spin texture with large momentum-dependent spin splitting. These findings point out a new direction for exploring valence–polarity–spin correlative interactions via topological ferroelectricity in metallic systems with structural asymmetry.

Topological states of matter, such as topological insulators,[1] Weyl semimetals,[2] and magnetic skyrmions,[3] have attracted tremendous attention for their intriguing physical properties and promising applications in spintronic, energy conversion, and memory devices. Following this tide, topological polar configurations in ordinary ferroelectric insulators have been discovered in a number of low-dimensional ferroelectric nanostructures.[4–6] In the 1960s, Anderson and Blount[7] proposed the concept of "ferroelectric metal", which offers exciting opportunities for exploring exotic phases and emergent phenomena in materials, for example, antisymmetric spin–orbit interactions in superconductors and ultrahigh magnetoresistance.[8,9] In recent years, a number of ordinary ferroelectric metals have been unveiled one after another.[10–12] However, topological ferroelectric metal has never been reported so far.

It is known that ferroelectric materials have polar point groups and exhibit bistable polarity along the unique polar axes.[13,14] In contrast, non-centrosymmetric (chiral and nonpolar) point groups allow for the presence of multiple local polar axes, which may facilitate the construction of topological order of polarity.[15] A number of electrocatalytic transition metal compounds, for example, WP_2 (Space group $Cmc2_1$)[9] and Ni_2P ($P\bar{6}2m$),[16–18] aroused our great curiosity because of their coexisting structural non-centrosymmetry with metallicity and the assignable non-unique valence states that relate to their nontrivial stoichiometry. Here, by focusing on electron-lattice-polarity correlations in Ni_2P, our

Dr. X.-K. Wei, Prof. R. E. Dunin-Borkowski
Ernst Ruska-Centre for Microscopy and Spectroscopy with Electrons and Peter Grünberg Institute
Forschungszentrum Jülich GmbH
Jülich 52425, Germany
E-mail: x.wei@fz-juelich.de

The ORCID identification number(s) for the author(s) of this article can be found under https://doi.org/10.1002/adma.202003479.

DOI: 10.1002/adma.202003479

Dr. G. Bihlmayer, Prof. S. Blügel
Peter Grünberg Institute and Institute for Advanced Simulation
Forschungszentrum Jülich GmbH and JARA
Jülich 52425, Germany

X. Zhou, Prof. W. Feng
Key Laboratory of Advanced Optoelectronic Quantum Architecture and Measurement
Ministry of Education
School of Physics
Beijing Institute of Technology
Beijing 100081, China

Dr. Y. V. Kolen'ko, Dr. L. Liu
International Iberian Nanotechnology Laboratory (INL)
Braga 4715-330, Portugal

Dr. D. Xiong
State Key Laboratory of Silicate Materials for Architectures
Wuhan University of Technology
Wuhan 430070, China

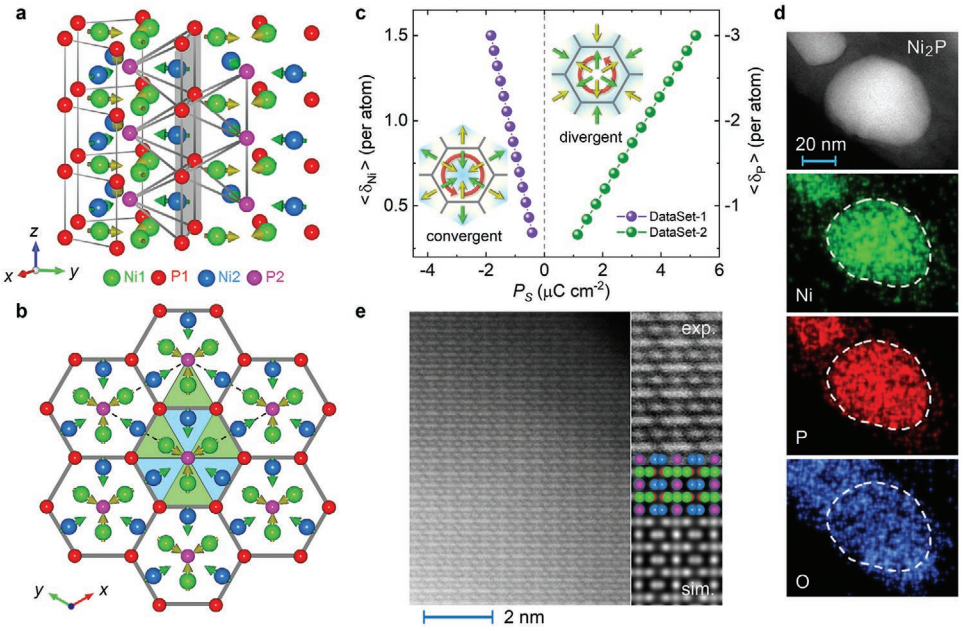

Figure 1. a) Alternate stacking of tail-to-tail polar tetrahedra (yellow arrows) and square pyramids (green arrows) along the *c* axis at an equivalently-transformed unit cell (ETUC) boundary, that is, sixfold-symmetric P1-containing {100} shadow plane. b) Relationship between a primitive unit cell (thin dashed lines) and an ETUC (thick solid lines) with a center-convergent dipole geometry viewed along the [001] direction. c) The polyhedral in-plane polarity plotted as a function of mean $<\delta_{Ni}>$ and $<\delta_P>$ for DataSet-1 and DataSet-2. The insets illustrate the real-space center-convergent and center-divergent topological configurations (winding number $n = 1$) associated with the anticlockwise integral contours (red circular arrows). d) HAADF-STEM image of Ni_2P nanoparticles and corresponding compositional maps of Ni, P, and O (from the oxide support). e) Atomic-resolution HAADF-STEM image recorded along the [100] direction. The inset shows magnified experimental and simulated images as well as a superimposed structure model.

symmetry-confined polarity analysis, electron energy-loss spectroscopy (EELS) measurement and first principles calculations reveal that asymmetric Ni_2P is a topological ferroelectric metal. Its switchable polyhedral polarity and coupling to degeneracy-lifting spin polarization present fascinating interactions in such asymmetric metallic materials.

Hexagonal Ni_2P, with lattice parameters of $a \approx 0.5859$ nm and $c \approx 0.3382$ nm, is comprised of Ni1-centered tetrahedra (Te) and Ni2-centered square-pyramids (Py) along the *c* axis (**Figure 1**a,b). In the presence of $\bar{6}$ rotation–inversion symmetry, only in-plane (IP) polarity is allowed to develop along the <100> directions, as evidenced by polar distortions of the polyhedra (Table S1, Supporting Information). For the sake of clarity, we re-shape the primitive unit cells (PUCs—dashed lines) into equivalently transformed unit cells (ETUCs—thick solid lines) with hexasymmetry (Figure 1b). The polyhedral polarity is then seen to form head-to-head and tail-to-tail charged configurations at P2-centered axes and ETUC boundaries within the unit cell, respectively. Studies on ordinary ferroelectrics have shown that charged domains with unequal polarization could destabilize the unit-cell-scale wall structures.[19] This indicates that a balance of tetrahedral-pyramidal polarity is a prerequisite for stabilization of the Ni_2P phase structure.

By taking into account the atomic sites, polyhedral coordination and elemental valence states (set as variables), we establish a series of symmetry equations to balance the polyhedral polarity of Ni_2P along the IP and out-of-plane (OP) directions. The bond dipole moment (*D*),[20] which is sensitive to bond length, elemental electronegativity difference, and coordination atom number, was first calculated to describe the polarity of the polyhedra in Ni_2P.

$$D_{\mathrm{Te(IP)}} = \left(\delta_{\mathrm{P1}}/9 + 2\delta_{\mathrm{P2}}/9 + x_1\delta_{\mathrm{Ni1}}\right)(a+b) \tag{1}$$

$$D_{\mathrm{Py(IP)}} = \left(2\delta_{\mathrm{P1}}/9 + x_2\delta_{\mathrm{Ni2}}\right)(a+b) \tag{2}$$

$$D^{j}_{\mathrm{Te(OP)}} = n_j\left(\delta_{\mathrm{P1}}/9 + \delta_{\mathrm{P2}}/9 + \delta_{\mathrm{Ni1}}/2\right)c \tag{3}$$

$$D^{\mathrm{j}}_{\mathrm{Py(OP)}} = m_j\left(4\delta_{\mathrm{P1}}/9 + \delta_{\mathrm{P2}}/9 + \delta_{\mathrm{Ni2}}\right)c \tag{4}$$

where D_{Te} and D_{Py} are the dipole moments of the polyhedra, x_1 (= y_1) and x_2 (= y_2) are the fractional coordinates of the Ni1 and Ni2 atoms, P atoms are located at fixed positions (see Table S1, Supporting Information) and the variable δ_i (i = Ni or P) is the valence state of Ni or P, respectively. Along the *z* axis, we noticed that m_j = ..., –1, 0, 1, 2, 3, ... for the pyramids and n_j = ..., –1, 1, 3, 5, ...for the tetrahedra with respect to locations of the polyhedra (Figure S1a, Supporting Information). In the basal plane, a balance of polyhedral polarity yields the expression

$$D_{\mathrm{Te(IP)}} = -D_{\mathrm{Py(IP)}} \tag{5}$$

For a tetrahedron that is sandwiched by a pair of pyramids along the *z* axis, we have

$$\frac{1}{2}D^{j-1}_{\mathrm{Py(OP)}} + \frac{1}{2}D^{j+1}_{\mathrm{Py(OP)}} = D^{j}_{\mathrm{Te(OP)}} \tag{6}$$

or

$$\frac{1}{2}D^{j-1}_{\mathrm{Te(OP)}} + \frac{1}{2}D^{j+1}_{\mathrm{Te(OP)}} = D^{j}_{\mathrm{Py(OP)}} \quad (7)$$

for a pyramid sandwiched by a pair of tetrahedra. We notice that the relation $m_{j-1} + m_{j+1} = n_j$ always holds. Together with the electroneutrality of the unit cell,

$$3\delta_{\mathrm{Ni1}} + 3\delta_{\mathrm{Ni1}} + 2\delta_{\mathrm{P1}} + \delta_{\mathrm{P2}} = 0 \quad (8)$$

we obtain analytic solutions to the equations. It is found that the valence states of Ni (δ_{Ni}) and P (δ_{P}) and separation of positive-negative charge centers for the polyhedra are linearly dependent on the fractional coordinates of Ni atoms in the *ab* plane (see Experimental Section). For the experimentally determined DataSet-1 (Ni1: $x_1 = y_1 = 0.7425$; Ni2: $x_2 = y_2 = 0.4043$),[16] we obtain $\delta_{\mathrm{Ni1}} = -0.427\delta_{\mathrm{P1}}$, $\delta_{\mathrm{Ni2}} = -0.547\ \delta_{\mathrm{P1}}$, and $\delta_{\mathrm{P2}} = 0.923\ \delta_{\mathrm{P1}}$ and separation of charge centers at $d_{\mathrm{c\text{-}Te}} = -1.45$ pm and $d_{\mathrm{c-Py}} = 1.14$ pm. For a mean nickel valence of $<\delta_{\mathrm{Ni}}> = 0.5$, the Ni and P valences are $\delta_{\mathrm{Ni1}} = 0.439$, $\delta_{\mathrm{Ni2}} = 0.561$, $\delta_{\mathrm{P1}} = -1.026$, and $\delta_{\mathrm{P2}} = -0.947$. The polyhedral polarity per unit volume (V_0 is volume of the unit cell), with $P_S = 6D/V_0 = -0.61\ \mu\mathrm{C\ cm^{-2}}$, forms a center-convergent geometry within the ETUC (Figure 1c).

As the Ni coordinates change to $x_1 = y_1 = 0.7432$ for Ni1 and $x_2 = y_2 = 0.4054$ for Ni2 (DataSet-2),[21] with the Ni1 and Ni2 atoms individually shifted by ≈0.42 pm and ≈0.66 pm, the polyhedral polarity is reversed and the charge centers are separated by $d_{\mathrm{c\text{-}Te}} = 3.75$ pm and $d_{\mathrm{c\text{-}Py}} = -3.00$ pm, respectively. Correspondingly, the polyhedral polarity with $P_S = 1.59\ \mu\mathrm{C\ cm^{-2}}$ at $<\delta_{\mathrm{Ni}}> = 0.5$ forms a center-divergent geometry. With increasing elemental valence state, the polyhedral polarity increases monotonically (Figure 1c). According to the theory of topological defects,[15] the IP center-convergent and center-divergent electric dipoles therefore form topological configurations in the order-parameter space of polarity. Given the homotopic relation of dipole counter maps per unit cell along the OP direction, this gives rise to a winding order $n = \frac{1}{2\pi}\oint d\theta = 1$ (where $d\theta$ is the angular change between neighboring polar vectors) for both cases and a globally null polarization in the crystal (Figure S1b–g, Supporting Information).

It is intriguing to find out the intimate polarity–valence correlation in non-centrosymmetric Ni_2P. In order to further affirm validity of the symmetry equations in this system, we measured the elemental valence states experimentally using EELS, which records information about the unoccupied local density of states (DOS) of excited atoms. Compositional analysis (Ni:P ≈ 2:1) by energy-dispersive X-ray spectroscopy (EDX) and atomic-resolution high-angle annular dark-field scanning transmission electron microscopy confirmed the identity of the structural phase (Figure 1d,e; Figure S2, Supporting Information). With respect to the elemental Ni standard, a positive chemical shift by 1.3 eV is observed for the Ni $L_{2,3}$ core edges (corresponding to a 2p → 3d dipole transition),[22] indicating the oxidation of Ni in the phosphide (**Figure 2**a). The empirical white-line intensity method, which is weakly dependent on local coordination geometry and bonding type,[23,24] was employed to probe the 3d electron occupancy ($n_{3\mathrm{d}}$) of Ni (see Experimental Section).

After subtraction of a stepped background and an oxidized surface signal (marked by asterisks in Figure 2a,b), our measurement provides a value of $n_{3\mathrm{d}} = 8.49$ for Ni in Ni_2P. Considering the hybridization of the d-band with the conduction band[25] and all possible $3d^{10-q}4s^q$ configurations, we obtain a range of $0.31 \le \delta_{\mathrm{Ni}} = 10-q-n_{3\mathrm{d}} \le 1.51$ for the Ni valence in the phosphide (inset in Figure 2a; Figure S3a,b, Supporting Information). Referring to the Ni^0 standard ($3d^94s^1$), the valence of Ni is determined to be $\delta_{\mathrm{Ni}} = 0.51 \pm 0.09$. Atomic-resolution EELS experiments reveal that the Ni valences are $\delta_{\mathrm{Ni1}} = 0.41 \pm 0.10$ and $\delta_{\mathrm{Ni2}} = 0.61 \pm 0.10$ (Figure 2b; Figure S4, Supporting Information). These values, reflecting the coordination discrepancy of Ni1 and Ni2 in the compound,[26] are in good agreement with solutions to the polarity symmetry equations.

Analogously, abrupt P *K* edges (peak A: 1s → 3p, peak B: 1s → P-3p/Ni-4p dipole transition[27]) were collected in our experiments for valence determination (Figure 2c; Figure S3c,d, Supporting Information). Defining the intersection of the profile slope with the energy axis as the onset energy, we see that the P *K* edge in the phosphide shifts negatively by 1.2 eV compared with the P^0 standard (Figure 2c). This is in sharp contrast to the phosphate (P^{5+}) standard, which shifts positively by 8.1 eV. The proximity of the P *K* edge onset to the P^0 standard suggests that P is weakly charged in the phosphide. In order to quantify the P valence state, we analyzed X-ray photoelectron spectroscopy (XPS) data for a wide range of P-containing compounds,[26,28–44] including phosphates, phosphites, and phosphides (see Table S2, Supporting Information). We find that the P-$2p_{3/2}$ binding energy (E_{B}) and the P valence (δ_{P}) form a bowknot-shaped chart with the node locating at the position of the P^0 standards (Figure 2d). By deducting the constant energy differences, for example, the 1s → $2p_{3/2}$ energy level gap (see Experimental Section), the XPS relation chart becomes applicable to the EELS *K* edges and the P valence in Ni_2P is determined to be in the range $-3.0 \le \delta_{\mathrm{P}} \le -0.62$, which is in good agreement with the values derived from the polarity symmetry equations.

On the basis of the experimental validation, first-principles calculations were performed to explore the switching mechanism of polyhedral polarization. In a fully relaxed condition, that is, $a = a_0$, the center-convergent topology has the most stable state and the polyhedral polarity is $P_S = 8.7\ \mu\mathrm{C\ cm^{-2}}$ at a fixed value of $<\delta_{\mathrm{Ni}}> = 0.5$ (see Experimental Section). In the presence of isotropic IP compressive strain, we find that the Ni1 and Ni2 atomic coordinates in Ni_2P linearly couple with each other, both of which increase monotonically with an increase of the compressive strain (**Figure 3**a; Figure S5a, Supporting Information). As the shifts of Ni1 and Ni2 atoms individually exceed 2.0 and 1.6 pm, the polyhedral polarization is reversed after exceeding a critical value of $a = 0.98a_0$ (Figure 3b). Correspondingly, the convergent-type topological configuration changes to divergent-type when $a < 0.98a_0$, for example, $P_S = 14.8\ \mu\mathrm{C\ cm^{-2}}$ at $a = 0.95a_0$. By monitoring local charges in the atomic spheres and considering the Ni valences determined from the experiments, our first principles calculation also reproduces the reversal of polyhedral polarity under the straining conditions (Figure S5b, Supporting Information). Meanwhile, we found that the shift of Wannier functions as a function of a/a_0 is consistent with the atomic shifts.

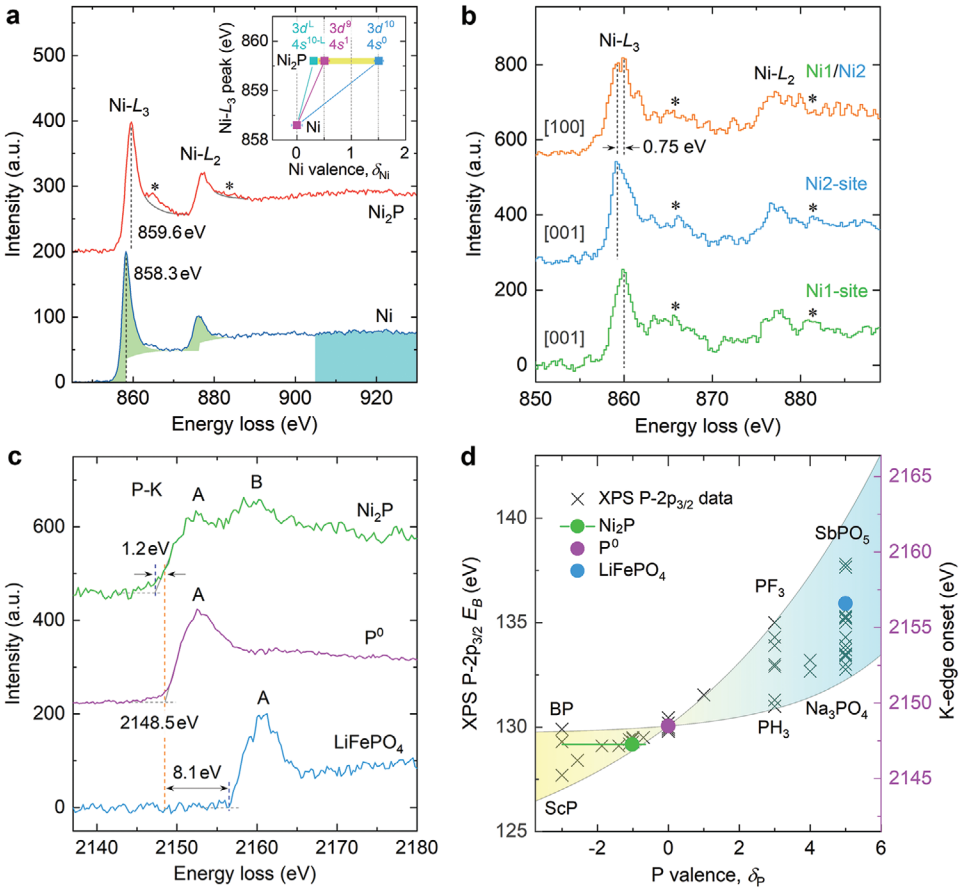

Figure 2. a) Core-loss spectra for Ni $L_{2,3}$ in Ni_2P and a Ni^0 standard, with the L_3 peaks marked by dashed lines. The white line intensity (green) was integrated and normalized by a 50 eV energy window (cyan) for n_{3d} measurement with $L = 8.8$ (see Experimental Section). b) Atomically resolved Ni $L_{2,3}$ edges recorded along [100] and [001] directions. c) P K edges in Ni_2P and in P^0 and $LiFePO_4$ standards, with onsets defined by the intersections of slopes (gray solid lines) with the energy axis (gray dashed lines). d) Bowknot-shaped binding energy (E_B) plotted as a function of P valence (δ_P) from XPS P-2$p_{3/2}$ data of P-containing compounds (see Table S2, Supporting Information). Replication of the E_B–δ_P relation to the P K edges referring to the P^0 standards quantifies the δ_P range (solid green line) in Ni_2P. The green circle marks $\delta_P = -1.02$.

By varying the Ni1 atomic site step by step and relaxing the Ni2 atoms, or vice versa, the system energy is observed to change in a parabolic manner. As a function of the Ni1 and Ni2 fractional coordinates, we see that the applied compressive strain creates a bilinear double-well potential together with the fully relaxed state ($a = a_0$) (Figure 3c,d). Specifically, as the applied strain exceeds the critical value of $\varepsilon = (a\text{-}a_0)/a_0 = -2\%$, the tunable bilinear double-well potential corresponds to the reversible polarization states of the polyhedra, resembling that in ordinary ferroelectrics such as $Hf_{0.5}Zr_{0.5}O_2$.[13] In the presence of compressive strain, our calculation also evidences a dramatic change of the 3D Fermi surfaces resulting from volume contraction and associated polarity reversal of the polyhedra (Figure 3e,f). The calculated DOS indicates that the metallic conductivity is dominated by Ni—Ni bonding from the neighboring polyhedra, which applies to the compressively strained situation as well (Figures S6 and S7, Supporting Information).

In ordinary ferroelectric semiconductors, it is known that inversion-symmetry breaking is intimately correlated with Rashba physics.[45] To further corroborate the topological polarization presented above, spin–orbit interaction was considered in our calculations. As a result of the absence of structural inversion symmetry in Ni_2P, a complicated momentum-dependent lifting of spin degeneracy of the electronic states is established. Specifically, some electronic states with finite k_z and $k_{||}$, sensing the switchable local IP polarization at specific straining conditions, are presented for comparison (**Figure 4**a–c). On the one hand, we find that the spin–orbit coupling induces spin splitting of bands in the range of 20 to 100 meV, reaching the order of magnitude of Rashba-type spin splitting of the Au (111) surface state.[46] On the other hand, from the z component of spin integrated over all atoms, we clearly see changes of the spin polarization with reversal of the polyhedral polarity, for example, the states at –0.8 eV near the zone boundary. Even when the local polarization is compensated, that is, at $a = 0.98a_0$, the spin splitting remains finite. This behavior is analogous to the "hidden spin polarization" observed in an inversion-symmetric crystal, which allows for these effects despite complete compensation of the lattice polarization.[47] Our results show that apart from semiconductors, the Rashba effect with substantial spin splitting is also observable in metals such as Ni_2P. This modifies the Fermi surface states (Figure 4e,f) and may consequently couple to the transport properties.

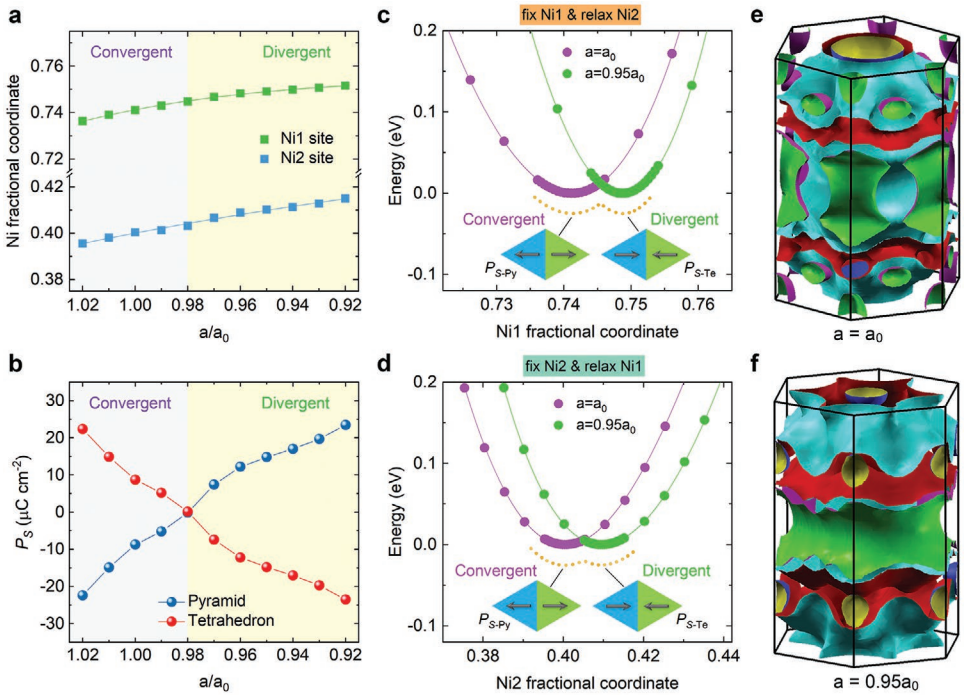

Figure 3. a,b) Changes of Ni fractional coordinates and polyhedral polarization at $<\delta_{Ni}> = 0.5$ plotted as a function of in-plane strain with respect to the fully relaxed condition ($a = a_0$), respectively. The boundary corresponds to reversal of the polyhedral polarization at $a = 0.98\ a_0$. c) Ground state energy change obtained by fixing the Ni1 atomic sites and relaxing the Ni2 sites at $a = a_0$ and $a = 0.95a_0$, respectively. d) Ground state energy change obtained by fixing the Ni2 atomic sites and relaxing the Ni1 sites at $a = a_0$ and $a = 0.95a_0$, respectively. The insets illustrate the change in topological polarity (pyramids–blue; tetrahedra–green) corresponding to the tunable double-well potential (yellow dotted lines). e,f) 3D plots of the Fermi surface (without spin–orbit coupling) for $a = a_0$ and $a = 0.95a_0$, respectively. The three sheets are annotated by green/magenta, cyan/red, and blue/yellow in terms of increasing order of the band index.

The presence of switchable local electric polarization and the similarity to a double-well potential (Figure 3c,d) indicate that the asymmetric Ni_2P shows an analogy to the ordinary ferroelectric semiconductors.[13] Nevertheless, the coexistence of topological polarity with metallicity distinguishes the nonpolar Ni_2P from the ordinary ferroelectrics, which are insulators and undergo phase transitions. Its unique structural, electrical, and spin-splitting properties therefore lead us to define a new material category—topological ferroelectric metal. It is noteworthy that the rotation–inversion symmetry plays an important role in enabling the coexistence of structural asymmetry with metallicity.[48] On the one hand, the unique stacking of acentric polyhedra, allowing IP polar displacements of Ni cations, constructs the unit-cell-scale short-range topological polar order in real space, whose long-range correlation is implemented by lattice translational symmetry. On the other hand, the Ni cations in the polyhedral cages form a 3D bonding network through the Ni—Ni bonds, which are responsible for the bulk conductivity (see Figures S6 and S7, Supporting Information). As a result of the dual roles of the Ni cations, the conflicting constraints to electron behavior in insulators are lifted in such systems.

In summary, the discovery of topological ferroelectricity in metallic nickel phosphide opens up a novel material category—topological ferroelectric metal. Similar topological behavior is expected to be present in binary and ternary pnictides,[49] chalcogenides,[22] and oxides that possess nonpolar (–4, –42 m, –6, –62 m, and –43 m), chiral and chiral-polar (1, 2, 3, 4, 6, 222, 422, 622, 32, 23, and 432) point groups. From a physics perspective, our findings provide a motivation for exploring interactions of real-space topological ferroelectricity with superconductivity[50] and ferromagnetism,[51] for example, in magnetic Fe_2P, which is structurally isomorphic to Ni_2P. Furthermore, the revealed spin polarization suggests the importance of considering spin–orbit interaction for deciphering reaction pathways[52] during electrochemical energy conversion using such catalytic materials.

Experimental Section

Sample Synthesis and Specimen Preparation: The Ni_2P nanoparticles on carbon paper and nanosheets on Ni foam were prepared by gas-transport phosphorization procedures under inert gas atmospheres. More synthetic details, X-ray diffraction and relevant characterization were presented elsewhere.[53–55] Scanning electron microscopy (JEOL, JSM-7400F) and STEM were used for morphological characterization. For TEM observations, a piece of Ni_2P/carbon paper was crushed using an agate mortar in ultrapure water. The suspension solution was dropped onto a Cu grid, dried on a plate oven (≈60 °C) and then cooled to room temperature. The nanosheets on Ni foam were first scraped using a blade. Then the above procedure was applied. The elemental Ni standard was prepared using a focused ion beam system (FEI Helios Nanolab 400s).

Structural, Electrical Characterization, and EELS, EDX Experiments: In these experiments, the phase structures of the nickel phosphides were usually examined using EDX and selected area electron diffraction before performing EELS experiments. The Dr. Probe software package was used

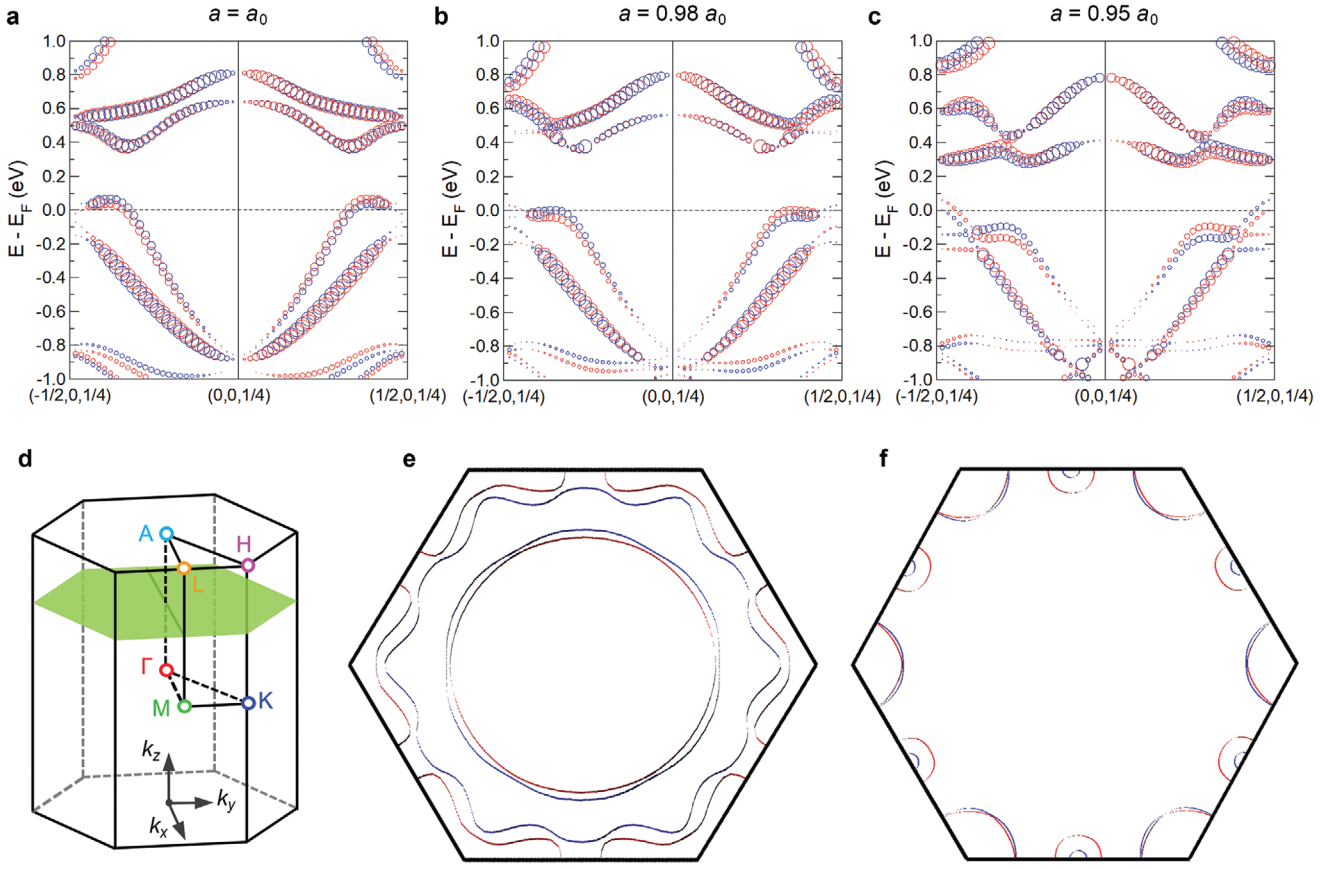

Figure 4. a–c) The most pronounced spin-splitting band structures near the Fermi level of Ni_2P for $a/a_0 = 1.0$, 0.98 and 0.95 occur along a line halfway between ΓM and AL, respectively. The size and sign of the *z* component of the spin polarization are indicated by the size and color of the symbols (blue—positive, red—negative). d) Illustration of the Brillouin zone with annotation of the high symmetry points and the (0 0 1/4)* plane (green). e,f) The Fermi surface cuts halfway between the ΓKM and AHL planes for the $a/a_0 = 1.0$ and 0.95 situations, respectively.

for image simulation,[56] and CrystalMaker and VESTA software packages were used for drawing the crystal structures. Electrical transport measurements showed that the Ni_2P exhibits metallic conductivity with a resistivity of ≈30 μΩ cm at room temperature.[57] An FEI Titan 80–200 ChemiSTEM microscope, which was equipped with a Super-X energy-dispersive X-ray spectrometer, STEM annular detectors and a Gatan Enfinium ER (model 977) spectrometer with DUAL EELS option (allowing calibration of core-loss spectra by low-loss spectra), was used to collect EDX and EELS results. The EEL spectra were collected using a convergence semi-angle of 24.7 mrad and a collection semi-angle of 29 mrad at a dispersion of 0.25 eV per pixel. The energy resolution was 1.25 eV based on the full width at half maximum of the zero-loss peak. As a result of surface oxidation, shoulder peaks beside the Ni $L_{2,3}$ edges were recorded from the phosphide.[58]

Valence State Quantification: The white line intensity method is used to determine the 3d electron occupation and oxidation state of Ni. Apart from power law background subtraction, the Ni $L_{2,3}$ spectra are deconvoluted using the Fourier-ratio method[59] to remove multiple scattering components when necessary, that is, when the specimen thickness $t/\lambda_p > 0.35$ (where the mean free path λ_p is ≈100 nm). After the removal of a continuum background modeled by the Hartree–Slater step function with a step height ratio of 3.3:1 at the peaks,[60] the white line intensities of the L_3 and L_2 edges are integrated and normalized by a 50 eV continuum energy window (starting 50 eV above the L_3 edge onset), defined as I_{3d}. As a calibration, the quality of the empirical formula

$$I_{3d} = 1.06(1 - 0.094 n_{3d}) \quad (9)$$

for obtaining the 3d electron occupancy is examined for the Ni^0 standard, for which the $3d^9 4s^1$ configuration has the lowest energy. This measurement reveals that $n_{3d} = 8.77$ for the Ni^0 standard, which is in an excellent agreement with a previous ($3d^{8.8}4s^{1.2}$) report.[24,25] On this basis, the n_{3d} in the phosphides is systematically calculated together with removal of the oxidized surface signal.

Comparison of XPS with EELS: The photoelectron signal from XPS originates from the excitation of inner shell electrons (core electrons) to the vacuum level. For EELS, the core electrons are excited into well-defined empty states, in analogy to X-ray absorption spectroscopy[26] and Auger electron spectroscopy.[29] The P $L_{2,3}$ edges correspond to transitions of $2p_{1/2}$ and $2p_{3/2}$ electrons into empty 3d orbitals, while the E_B values of the same 2p orbitals are detected using XPS. Apart from the $1s \rightarrow 2p_{3/2}$ energy level difference (≈2014 eV), the different final states measured using XPS, involving a reference of E_B ($e\phi_{spectrometer}$, an energy gap between the vacuum level and E_F of the spectrometer) from that of EELS could also result in a constant difference[26,29] between E_B of $2p_{3/2}$ and the *K* edge onset of EELS. An energy shift (by a few eV) caused by instrument-dependent dispersion differences (per pixel) and onset-energy definitions are also considered. The XPS-P $2p_{3/2}$ data[26,28–44] from phosphates, phosphites, oxides, halides, phosphides, etc. are summarized in Table S2, Supporting Information.

Winding Number: Analogous to the skyrmions,[61,62] by mapping the polyhedral polarity of an ETUC into a circular order-parameter space,[6,15,63] summation of the total angle changes gives rise to the winding number $n = \frac{1}{2\pi}\oint d\theta = 1$ for both convergent-type and divergent-type topological configurations of Ni_2P. This holds true for two

considerations, either a basic block (a layer of tetrahedral units plus a layer of pyramidal units), or two basic blocks (a layer of tetrahedral units versus a layer of pyramidal units), given the homotopic mappings of IP dipole counter maps along the OP direction.

Solution to Symmetry Equations of Polarity: By solving the symmetry equations, analytic solutions about valence state relationship between the elements and expression of separated charge centers ($d_{c\text{-}Te}$ vs $d_{c\text{-}Py}$) were obtained. In particular, each polyhedron was found to be electroneutral, that is, $D^j_{Te(OP)} = D^j_{Py(OP)} = 0$.

$$\delta_{Ni1} = \frac{2(1-3x_2)}{9(2-2x_1-x_2)}\,\delta_{P1} \tag{10}$$

$$\delta_{Ni2} = \frac{6x_1-5}{9(2-2x_1-x_2)}\,\delta_{P1} \tag{11}$$

$$\delta_{P2} = \frac{2x_1+4x_2-3}{2-2x_1-x_2}\,\delta_{P1} \tag{12}$$

$$d_{c-Te} = \left(\frac{2x_1+7x_2-4}{6x_2-2} - x_1\right)a \tag{13}$$

$$d_{c-Py} = \left(\frac{2(2-2x_1-x_2)}{5-6x_1} - x_2\right)a \tag{14}$$

where a is the lattice constant, and $d_{c\text{-}Te}$ versus $d_{c\text{-}Py}$ was irrelevant to the valence states. Taking into account the volume space occupied by the polyhedra, that is, $V_0/6$ where V_0 is the volume of the PUC or ETUC (see Figure S1, Supporting Information), the bond dipole moment could be converted to polarization, that is, $|P_S| = |6D/V_0|$. For clarity, changes in the quantities as a function of Ni1 and Ni2 fractional coordinates are shown in Figure S8, Supporting Information. For DataSet-2,[21] the valence relations were $\delta_{Ni1} = -0.444\delta_{P1}$, $\delta_{Ni2} = -0.555\ \delta_{P1}$, and $\delta_{P2} = 0.997\ \delta_{P1}$. At $<\delta_{Ni}> = 0.5$, $\delta_{Ni1} = 0.444$, $\delta_{Ni2} = 0.556$, $\delta_{P1} = -1.001$, and $\delta_{P2} = -0.998$. Referring to the Ni^0-$3d^L$ ($L = 8.8$)[25] configuration, that is, $<\delta_{Ni}> = 0.31$, the upper boundary solution to the equations yielded $<\delta_{Ni1}> = 0.274$, $<\delta_{Ni2}> = 0.346$, $<\delta_{P1}> = -0.640$, and $<\delta_{P2}> = -0.591$ for the two datasets. Referring to the $3d^{10}$ configuration, that is, $<\delta_{Ni}> = 1.50$, the lower boundary solution yielded $<\delta_{Ni1}> = 1.324$, $<\delta_{Ni2}> = 1.676$, $<\delta_{P1}> = -3.041$, and $<\delta_{P2}> = -2.918$. Considering the 3Ni1-2P1 and 3Ni2-1P2 constituent per unit cell, the solutions to the symmetry equations of polarity gave the valence range of $-3.0 \le \delta_P \le -0.616$.

First Principles Calculations: The theoretical work was performed based on first principles density functional theory implemented in the Vienna ab initio Simulation Package (VASP)[64] and the FLEUR code.[65] Where indicated, the spin-orbit coupling was considered in a self-consistent manner. The exchange-correlation effect was treated with the Perdew, Burke, and Ernzerhof functional.[66] An energy cutoff of 400 eV, with the energy convergence criterion set at 10^{-6} eV, was used in the VASP calculations. A Γ-centered k-mesh of $10 \times 10 \times 18$ was employed to converge the self-consistent field calculations of Ni_2P. For metallic Ni_2P, the Z_2 topological invariants[67] cannot be calculated, indicating that there is an essential difference between topological spin and topological polarity in the band structures. From the ab initio calculations, it was difficult to obtain local polarizations, but the trends can be followed by monitoring local charges in atomic spheres and using the polarity equations, the charge neutrality condition, Equation (8), and the experimentally-observed Ni valence as calibrating conditions. Specifically, the polarity ($\boldsymbol{D}$) of a bond formed by a pair of atoms (A, B) at positions (x_A, x_B) and with local charges (δ_A, δ_B) was expressed by $\boldsymbol{D} = (x_A - x_B)(\delta_A - \delta_B)$ so that

$$\boldsymbol{D}_{Py} = \left[4(1/2-x_2)(\delta_{P1}/9-\delta_{Ni2}) - x_2(\delta_{P2}/9-\delta_{Ni2})\right](a+b) \tag{15}$$

$$\boldsymbol{D}_{Te} = \left[2(1/2-x_1)(\delta_{P1}/9-\delta_{Ni1}) + 2(1-x_1)(\delta_{P2}/9-\delta_{Ni1})\right](a+b) \tag{16}$$

Assuming that the Ni valence was given by the deviation of charge inside the atomic sphere from a nominal value $\delta_{Ni} = \alpha(9-q_{Ni})$ and similarly $\delta_P = \beta(\theta - q_P)$, the constants α, β, and θ could be determined from $\boldsymbol{D}_{Py} = -\boldsymbol{D}_{Te}$, Equation (8) and $\delta_{Ni1} + \delta_{Ni2} = 1.0$ (see Figure S5, Supporting Information). It was seen that at the compensation point ($a/a_0 = 0.982$) the relations between the valences given in the main text were almost perfectly fulfilled.

Supporting Information

Supporting Information is available from the Wiley Online Library or from the author.

Acknowledgements

This work was supported by the European Union's Horizon 2020 research and innovation program through the CritCat Project under grant agreement No. 686053. X.Z. and W.F. acknowledge support from the National Natural Science Foundation of China (No. 11874085). The authors thank Dr. Qianli Ma and Dr. Katherine MacArthur for providing standard samples.

Open access funding enabled and organized by Projekt DEAL.

Conflict of Interest

The authors declare no conflict of interest.

Author Contributions

X.-K.W. conceived the idea and coordinated the study. R.D.-B. was responsible for the overall project. X.-K.W. carried out the electron microscopy experiments and analysis. G.B. performed first principles calculations with contributions from X.Z. and W.F. under the supervision of S.B. Y.V.K., D.X., and L.L. synthesized samples and performed X-ray diffraction. X.-K.W. and G.B. wrote the manuscript. All authors discussed the results and commented on the manuscript.

Keywords

electron energy loss spectroscopy, nickel phosphide, polyhedral polarization switching, strain engineering, topological ferroelectric metal

Received: May 21, 2020
Revised: August 21, 2020
Published online: October 7, 2020

[1] M. Z. Hasan, C. L. Kane, *Rev. Mod. Phys.* **2010**, *82*, 3045.
[2] G. B. Osterhoudt, L. K. Diebel, M. J. Gray, X. Yang, J. Stanco, X. Huang, B. Shen, N. Ni, P. J. W. Moll, Y. Ran, K. S. Burch, *Nat. Mater.* **2019**, *18*, 471.
[3] A. Fert, N. Reyren, V. Cros, *Nat. Rev. Mater.* **2017**, *2*, 17031.
[4] S. Das, Y. L. Tang, Z. Hong, M. A. P. Goncalves, M. R. McCarter, C. Klewe, K. X. Nguyen, F. Gomez-Ortiz, P. Shafer, E. Arenholz, V. A. Stoica, S. L. Hsu, B. Wang, C. Ophus, J. F. Liu, C. T. Nelson, S. Saremi, B. Prasad, A. B. Mei, D. G. Schlom, J. Iniguez, P. Garcia-Fernandez, D. A. Muller, L. Q. Chen, J. Junquera, L. W. Martin, R. Ramesh, *Nature* **2019**, *568*, 368.

[5] J. Ma, J. Ma, Q. Zhang, R. Peng, J. Wang, C. Liu, M. Wang, N. Li, M. Chen, X. Cheng, P. Gao, L. Gu, L. Q. Chen, P. Yu, J. Zhang, C. W. Nan, *Nat. Nanotechnol.* **2018**, *13*, 947.
[6] K. E. Kim, S. Jeong, K. Chu, J. H. Lee, G. Y. Kim, F. Xue, T. Y. Koo, L. Q. Chen, S. Y. Choi, R. Ramesh, C. H. Yang, *Nat. Commun.* **2018**, *9*, 403.
[7] P. W. Anderson, E. I. Blount, *Phys. Rev. Lett.* **1965**, *14*, 217.
[8] M. Smidman, M. B. Salamon, H. Q. Yuan, D. F. Agterberg, *Rep. Prog. Phys.* **2017**, *80*, 036501.
[9] N. Kumar, Y. Sun, N. Xu, K. Manna, M. Yao, V. Suss, I. Leermakers, O. Young, T. Forster, M. Schmidt, H. Borrmann, B. Yan, U. Zeitler, M. Shi, C. Felser, C. Shekhar, *Nat. Commun.* **2017**, *8*, 1642.
[10] Y. G. Shi, Y. F. Guo, X. Wang, A. J. Princep, D. Khalyavin, P. Manuel, Y. Michiue, A. Sato, K. Tsuda, S. Yu, M. Arai, Y. Shirako, M. Akaogi, N. L. Wang, K. Yamaura, A. T. Boothroyd, *Nat. Mater.* **2013**, *12*, 1023.
[11] Z. Fei, W. Zhao, T. A. Palomaki, B. Sun, M. K. Miller, Z. Zhao, J. Yan, X. Xu, D. H. Cobden, *Nature* **2018**, *560*, 336.
[12] T. H. Kim, D. Puggioni, Y. Yuan, L. Xie, H. Zhou, N. Campbell, P. J. Ryan, Y. Choi, J. W. Kim, J. R. Patzner, S. Ryu, J. P. Podkaminer, J. Irwin, Y. Ma, C. J. Fennie, M. S. Rzchowski, X. Q. Pan, V. Gopalan, J. M. Rondinelli, C. B. Eom, *Nature* **2016**, *533*, 68.
[13] M. Hoffmann, F. P. G. Fengler, M. Herzig, T. Mittmann, B. Max, U. Schroeder, R. Negrea, P. Lucian, S. Slesazeck, T. Mikolajick, *Nature* **2019**, *565*, 464.
[14] H. Lu, C.-W. Bark, D. Esque de los Ojos, J. Alcala, C. B. Eom, G. Catalan, A. Gruverman, *Science* **2012**, *336*, 59.
[15] N. D. Mermin, *Rev. Mod. Phys.* **1979**, *51*, 591.
[16] S. Rundqvist, *Acta Chem. Scand. (1947-1973)* **1962**, *16*, 992.
[17] E. J. Popczun, J. R. McKone, C. G. Read, A. J. Biacchi, A. M. Wiltrout, N. S. Lewis, R. E. Schaak, *J. Am. Chem. Soc.* **2013**, *135*, 9267.
[18] K. U. D. Calvinho, A. B. Laursen, K. M. K. Yap, T. A. Goetjen, S. Hwang, N. Murali, B. Mejia-Sosa, A. Lubarski, K. M. Teeluck, E. S. Hall, E. Garfunkel, M. Greenblatt, G. C. Dismukes, *Energy Environ. Sci.* **2018**, *11*, 2550.
[19] X.-K. Wei, Y. Yang, L. J. McGilly, L. Feigl, R. E. Dunin-Borkowski, C.-L. Jia, L. Bellaiche, N. Setter, *Phys. Rev. B* **2018**, *98*, 020102(R).
[20] Y. Inoue, *Energy Environ. Sci.* **2009**, *2*, 364.
[21] *Ni_2P Crystal Structure: Inorganic Solid Phases*, (Ed: P. Villars), Springer, Heidelberg, Germany **2012**.
[22] C. Yang, M. Y. Gao, Q. B. Zhang, J. R. Zeng, X. T. Li, A. P. Abbott, *Nano Energy* **2017**, *36*, 85.
[23] D. A. Muller, D. J. Singh, J. Silcox, *Phys. Rev. B* **1998**, *57*, 8181.
[24] D. H. Pearson, C. C. Ahn, B. Fultz, *Phys. Rev. B* **1993**, *47*, 8471.
[25] L. Hodges, H. Ehrenreich, N. D. Lang, *Phys. Rev.* **1966**, *152*, 505.
[26] P. E. R. Blanchard, A. P. Grosvenor, R. G. Cavell, A. Mar, *J. Mater. Chem.* **2009**, *19*, 6015.
[27] P. E. R. G. Blanchard, A. P. Cavell, G. Ronald, A. Mar, *Chem. Mater.* **2008**, *20*, 7081.
[28] X.-L. Zhou, J. M. White, *Surf. Sci.* **1989**, *221*, 534.
[29] R. Franke, T. Chassé, P. Streubel, A. Meisel, *J. Electron Spectrosc. Relat. Phenom.* **1991**, *56*, 381.
[30] A. P. W. Grosvenor, D. Stephen, R. G. Cavell, A. Mar, *Inorg. Chem.* **2005**, *44*, 8988.
[31] C. E. Myers, H. F. Franzen, J. W. Anderegg, *Inorg. Chem.* **1985**, *24*, 1822.
[32] V. Sudarsan, K. P. Muthe, J. C. Vyas, S. K. Kulshreshtha, *J. Alloy Compd.* **2002**, *336*, 119.
[33] A. A. Ogwu, T. Hellwig, *Int. J. Electrochem. Sci.* **2014**, *9*, 8299.
[34] X-ray Photoelectron Spectroscopy (XPS) Reference Pages, https://www.xpsfitting.com/search/label/Phosphorus (accessed: March 2019).
[35] X. W. Zhang, S. Y. Xu, G. R. Han, *Phys. Status Solidi A* **2004**, *201*, 2922.
[36] M. C. Traub, J. S. Biteen, D. J. Michalak, L. J. Webb, B. S. Brunschwig, N. S. Lewis, *J. Phys. Chem. C* **2008**, *112*, 18467.
[37] Z. Qi, W. Lee, *Tribol. Int.* **2010**, *43*, 810.
[38] M. C. Oliveira, A. M. B. do Rego, *J. Alloy Compd.* **2006**, *425*, 64.
[39] Y. Wang, P. M. A. Sherwood, *Surf. Sci. Spectra* **2002**, *9*, 99.
[40] Y. C. Lin, Y. Y. Chen, B. Y. Yu, W. C. Lin, C. H. Kuo, J. J. Shyue, *Analyst* **2009**, *134*, 945.
[41] K. Saravanan, M. V. Reddy, P. Balaya, H. Gong, B. V. R. Chowdari, J. J. Vittal, *J. Mater. Chem.* **2009**, *19*, 605.
[42] V. Venckutė, J. Miškinis, V. Kazlauskienė, T. Šalkus, A. Dindune, Z. Kanepe, J. Ronis, A. Maneikis, M. Lelis, A. Kežionis, A. F. Orliukas, *Phase Transitions* **2014**, *87*, 438.
[43] M. T. Edmonds, A. Tadich, A. Carvalho, A. Ziletti, K. M. O'Donnell, S. P. Koenig, D. F. Coker, B. Ozyilmaz, A. H. Neto, M. S. Fuhrer, *ACS Appl. Mater. Interfaces* **2015**, *7*, 14557.
[44] M. C. Righi, S. Loehlé, M. I. de Barros Bouchet, D. Philippon, J. M. Martin, *RSC Adv.* **2015**, *5*, 101162.
[45] D. Di Sante, P. Barone, R. Bertacco, S. Picozzi, *Adv. Mater.* **2013**, *25*, 509.
[46] S. LaShell, B. A. McDougall, E. Jensen, *Phys. Rev. Lett.* **1996**, *77*, 3419.
[47] X. Zhang, Q. Liu, J.-W. Luo, A. J. Freeman, A. Zunger, *Nat. Phys.* **2014**, *10*, 387.
[48] D. Puggioni, J. M. Rondinelli, *Nat. Commun.* **2014**, *5*, 3432.
[49] S. Anantharaj, S. R. Ede, K. Sakthikumar, K. Karthick, S. Mishra, S. Kundu, *ACS Catal.* **2016**, *6*, 8069.
[50] I. A. Sergienko, V. Keppens, M. McGuire, R. Jin, J. He, S. H. Curnoe, B. C. Sales, P. Blaha, D. J. Singh, K. Schwarz, D. Mandrus, *Phys. Rev. Lett.* **2004**, *92*, 065501.
[51] L. Lundgren, G. Tarmohamed, O. Beckman, B. Carlsson, S. Rundqvist, *Phys. Scr.* **1978**, *17*, 39.
[52] W. Mtangi, V. Kiran, C. Fontanesi, R. Naaman, *J. Phys. Chem. Lett.* **2015**, *6*, 4916.
[53] J. Xu, X.-K. Wei, J. D. Costa, J. L. Lado, B. Owens-Baird, L. P. L. Gonçalves, S. P. S. Fernandes, M. Heggen, D. Y. Petrovykh, R. E. Dunin-Borkowski, K. Kovnir, Y. V. Kolen'ko, *ACS Catal.* **2017**, *7*, 5450.
[54] X. G. Wang, Y. V. Kolen'ko, X. Q. Bao, K. Kovnir, L. F. Liu, *Angew. Chem., Int. Ed.* **2015**, *54*, 8188.
[55] X. K. Wei, D. Xiong, L. Liu, R. E. Dunin-Borkowski, *ACS Appl. Mater. Interfaces* **2020**, *12*, 21616.
[56] J. Barthel, *Ultramicroscopy* **2018**, *193*, 1.
[57] G. V. Samsonov, Y. B. Paderno, V. I. Lazorenko, P. A. Vityaz, *Powder Metall. Met. Ceram.* **1971**, *10*, 565.
[58] Z. Li, X. Dou, Y. Zhao, C. Wu, *Inorg. Chem. Front.* **2016**, *3*, 1021.
[59] F. Wang, R. Egerton, M. Malac, *Ultramicroscopy* **2009**, *109*, 1245.
[60] R. D. Leapman, L. A. Grunes, P. L. Fejes, *Phys. Rev. B* **1982**, *26*, 614.
[61] X. Z. Yu, Y. Onose, N. Kanazawa, J. H. Park, J. H. Han, Y. Matsui, N. Nagaosa, Y. Tokura, *Nature* **2010**, *465*, 901.
[62] Y. Nahas, S. Prokhorenko, L. Louis, Z. Gui, I. Kornev, L. Bellaiche, *Nat. Commun.* **2015**, *6*, 8542.
[63] J. Hong, G. Catalan, D. N. Fang, E. Artacho, J. F. Scott, *Phys. Rev. B* **2010**, *81*, 172101.
[64] G. Kresse, J. Furthmüller, *Comput. Mater. Sci.* **1996**, *6*, 15.
[65] The FLEUR code: https://www.flapw.de.
[66] J. P. Perdew, K. Burke, M. Ernzerhof, *Phys. Rev. Lett.* **1997**, *78*, 1396.
[67] W. Feng, J. Wen, J. Zhou, D. Xiao, Y. Yao, *Comput. Phys. Commun.* **2012**, *183*, 1849.